Electronic Supplementary Material (ESI) for Physical Chemistry Chemical Physics

ALD TiO_2 coated Silicon Nanowires for Lithium Ion Battery Anodes with enhanced Cycling Stability and Coulombic Efficiency

Elmira Memarzadeh Lotfabad[a], Peter Kalisvaart[a,*], Kai Cui[b], Alireza Kohandehghan[a], Martin Kupsta[b], Brian Olsen[a], David Mitlin[a,b,**]

a: University of Alberta Department of Chemical&Materials Engineering, 9107 116th Street, T6G 2V4, Edmonton AB, Canada

b: National Institute for Nanotechnology (NINT), NRC, 11421 Saskatchewan Dr., Edmonton, AB, T6G 2M9, Canada

Supporting Information

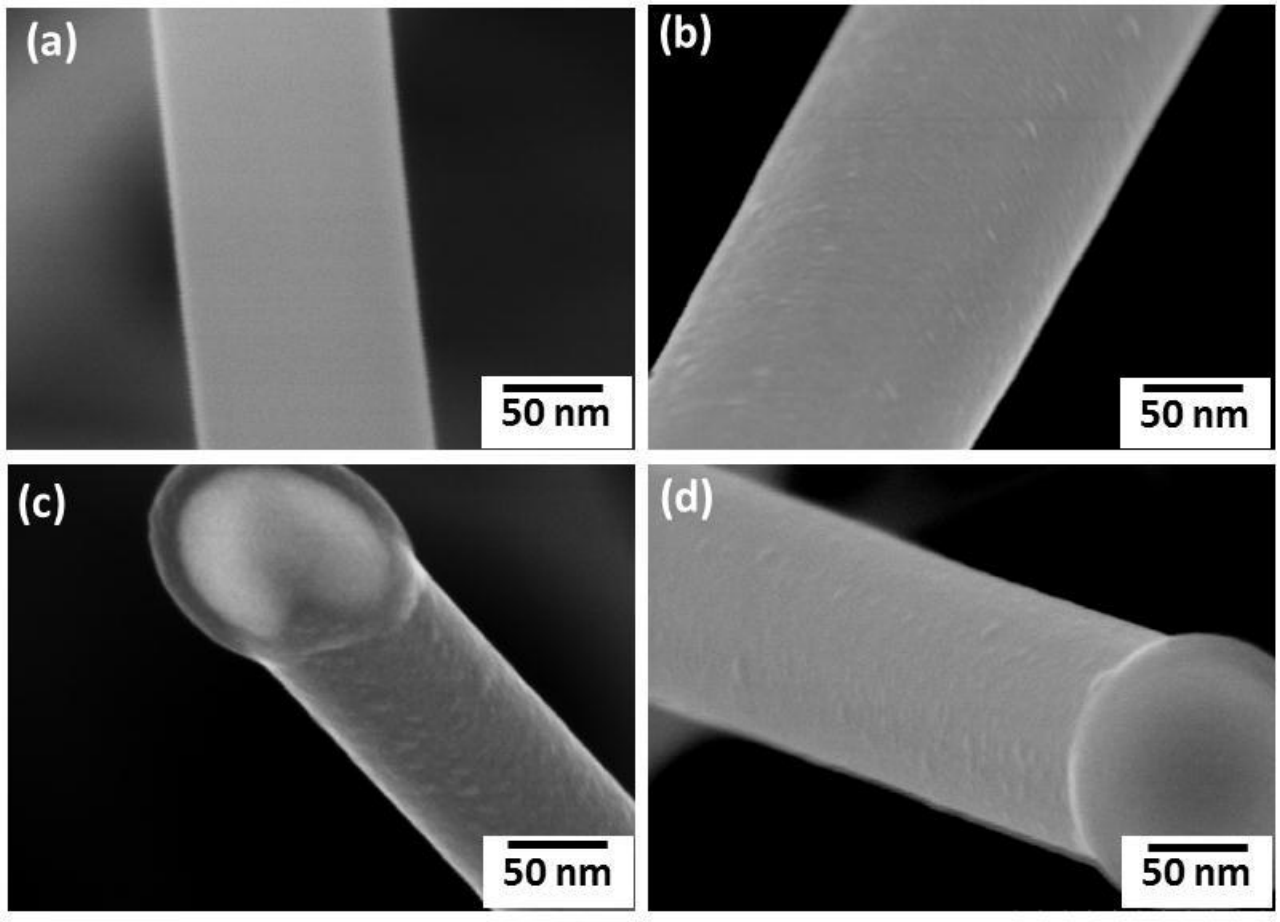

Figure S1: SEM images of (a) SiNWs, (b) (10)TiO_2-200/SiNWs, (c) (10)TiO_2-300/SiNWs, (d) (10)TiO_2-200(A)/SiNWs.

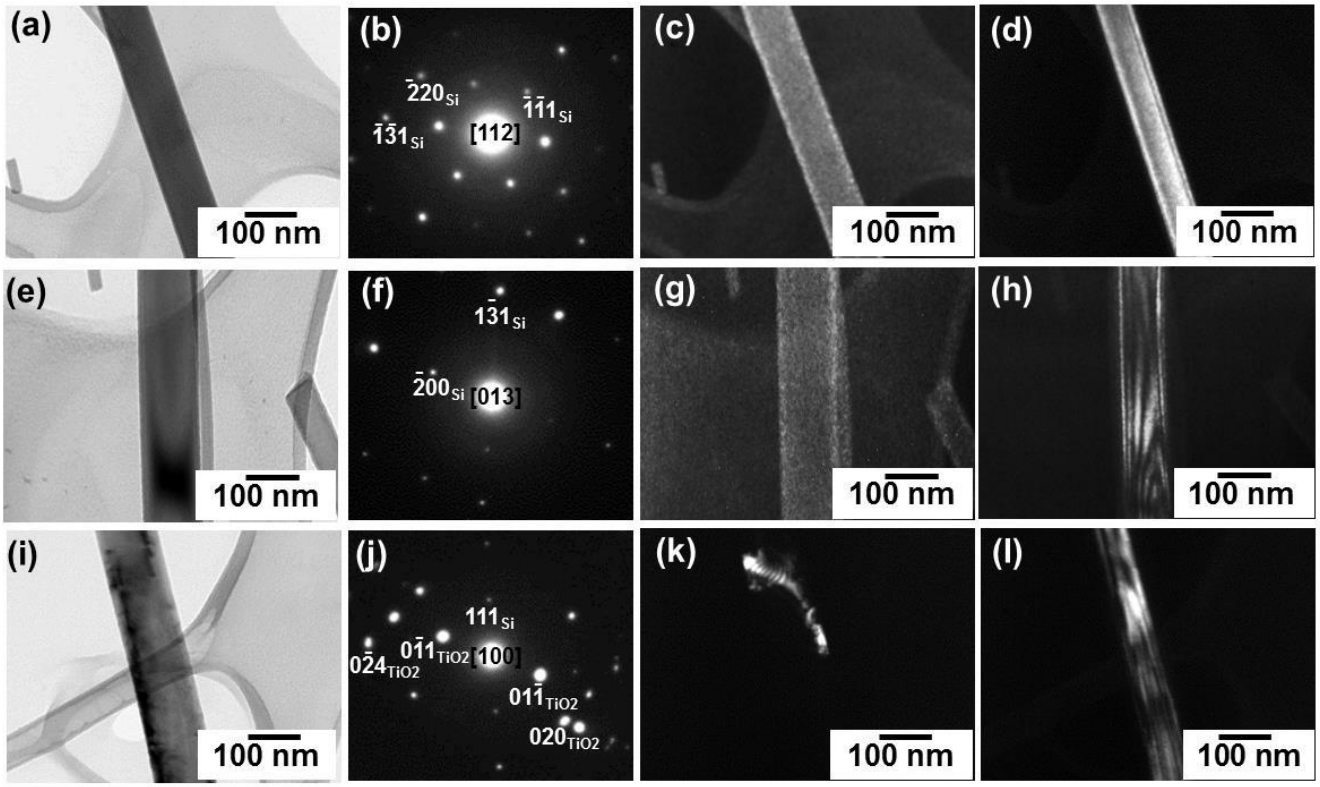

Figure S2. TEM micrographs of TiO_2 coated SiNWs. (a)-(d): (10)TiO_2-200/SiNWs. (a) Bright field micrograph, (b) corresponding indexed selected area diffraction (SAD), (c) dark field micrograph obtained using a portion of the diffuse halo of amorphous TiO_2 between the primary beam and the first set of Bragg reflections of Si, (d) dark field micrograph of the Si obtained using g =111_{Si} with the wire oriented near the 112 symmetric zone axis, (e)–(h): (10)TiO_2-300/SiNWs. (e) Bright field micrograph, (f) corresponding indexed SAD, (g) Dark field micrograph obtained using a portion of the diffuse halo of amorphous TiO_2 between the primary beam and the first set of Bragg reflections of Si, (h) dark field micrograph of the Si obtained using g=111_{Si}. (i)–(l): (10)TiO_2-200(A)/SiNWs. (j) Bright field micrograph, (j) corresponding indexed SAD showing the 011, 020 and 024 diffraction spots of anatase TiO_2, (k) dark field micrograph, obtained using g=011_{TiO2}, (l) dark field micrograph of the Si obtained using g =111_{Si}.

The microstructure of (10)TiO_2/SiNWs nanocomposites at different ALD deposition temperatures was examined by TEM and is presented in Figure S2. Figure S2a and e show the bright field micrographs of (10)TiO_2-200/SiNWs and (10)TiO_2-300/SiNWs, respectively. The corresponding SAD patterns (Figure S2b and f) consist of an overlay of a single crystal spot pattern of Si and a diffuse halo around the primary beam associated with amorphous TiO_2. The dark-field images in Figure S2c and g were taken using a portion of the diffuse halo between the primary beam and the first set of Si Bragg reflections and show the TiO_2 shell around the nanowire core. The SiNWs shown in Figure S2d and h are imaged using the g=111_{Si} reflection. After annealing treatment, the diffuse halo is gone and second spot pattern belonging to anatase

TiO_2 appears besides that of Si (Figure S2j). The dark field images in Figure S2k and l are taken from the $g=011_{TiO2}$ and $g=111_{Si}$ reflections, respectively.

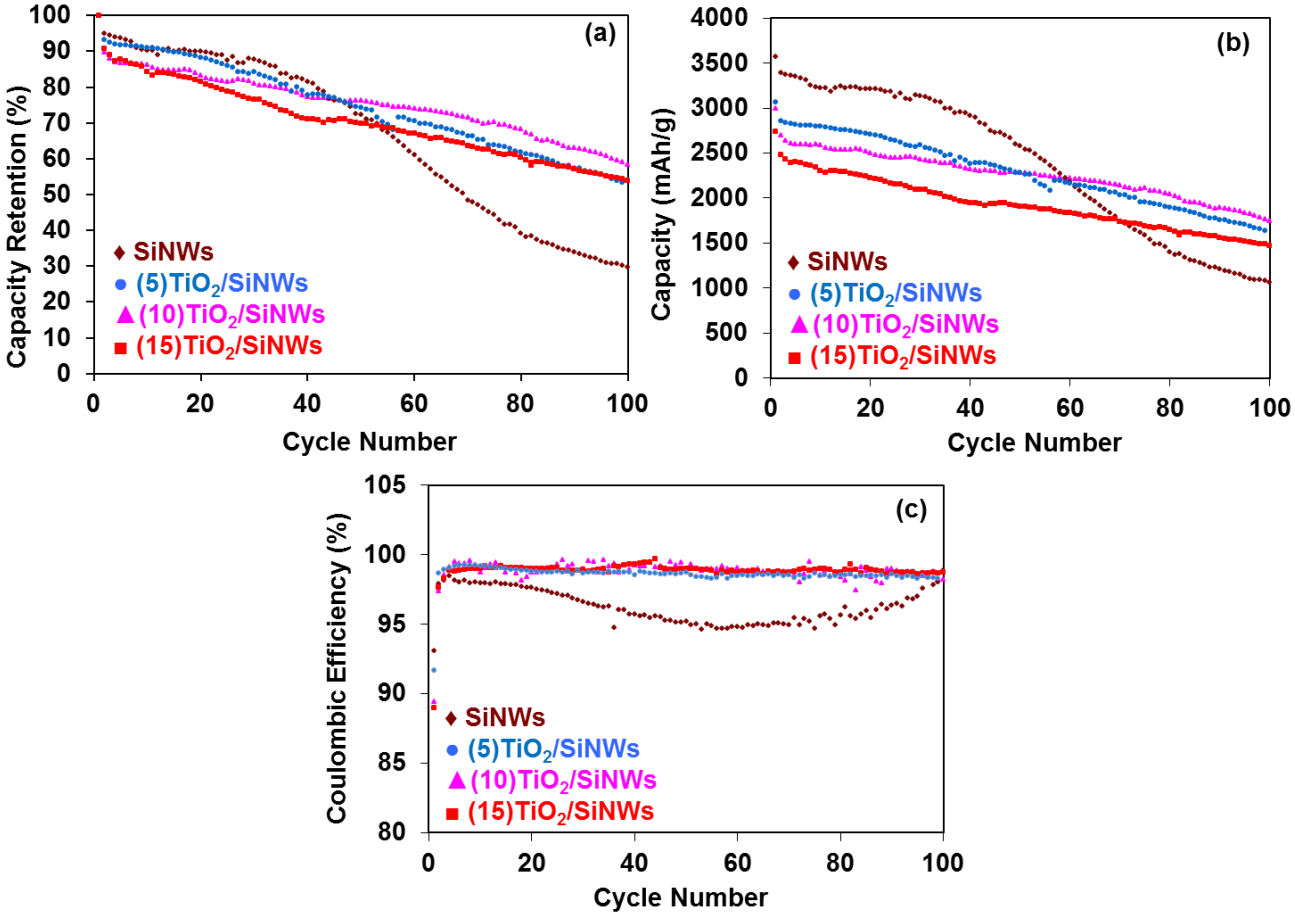

Figure S3. Capacity retention vs. cycle number, expressed as a percentage relative to the first cycle capacity, for bare and TiO_2-200/SiNWs nanocomposites at different TiO_2 thicknesses cycled at 0.1 C rate, (b) specific capacity in mAh/g and (c) corresponding coulombic efficiency.

Using identical deposition conditions, the effect of coating thickness was investigated for a deposition temperature of 200°C. Three (x)TiO_2-200/SiNWs composites were synthesized with x = 5, 10 and 15 nm and the results are shown in Figure S3. The cycling stabilities are quite similar in that none of the composites show the increase in the degradation rate starting around cycle 40 that iss observed for bare SiNWs in Figure S3a. (5)TiO_2-200/SiNWs has a slightly higher, albeit approximately constant, degradation rate than (10)TiO_2-200/SiNWs. (15)TiO_2-200/SiNWs has considerably lower capacity because of the higher added weight of TiO_2; 31 vs. 22 wt% when compared to (10)TiO_2-200/SiNWs. The coulombic efficiency is consistently ~99% for all three composites. (10)TiO_2-200/SiNWs has better stability than (5)TiO_2-200/SiNWs and higher capacity than (15)TiO_2-200/SiNWs and should be considered optimal with regard to the coating

thickness.

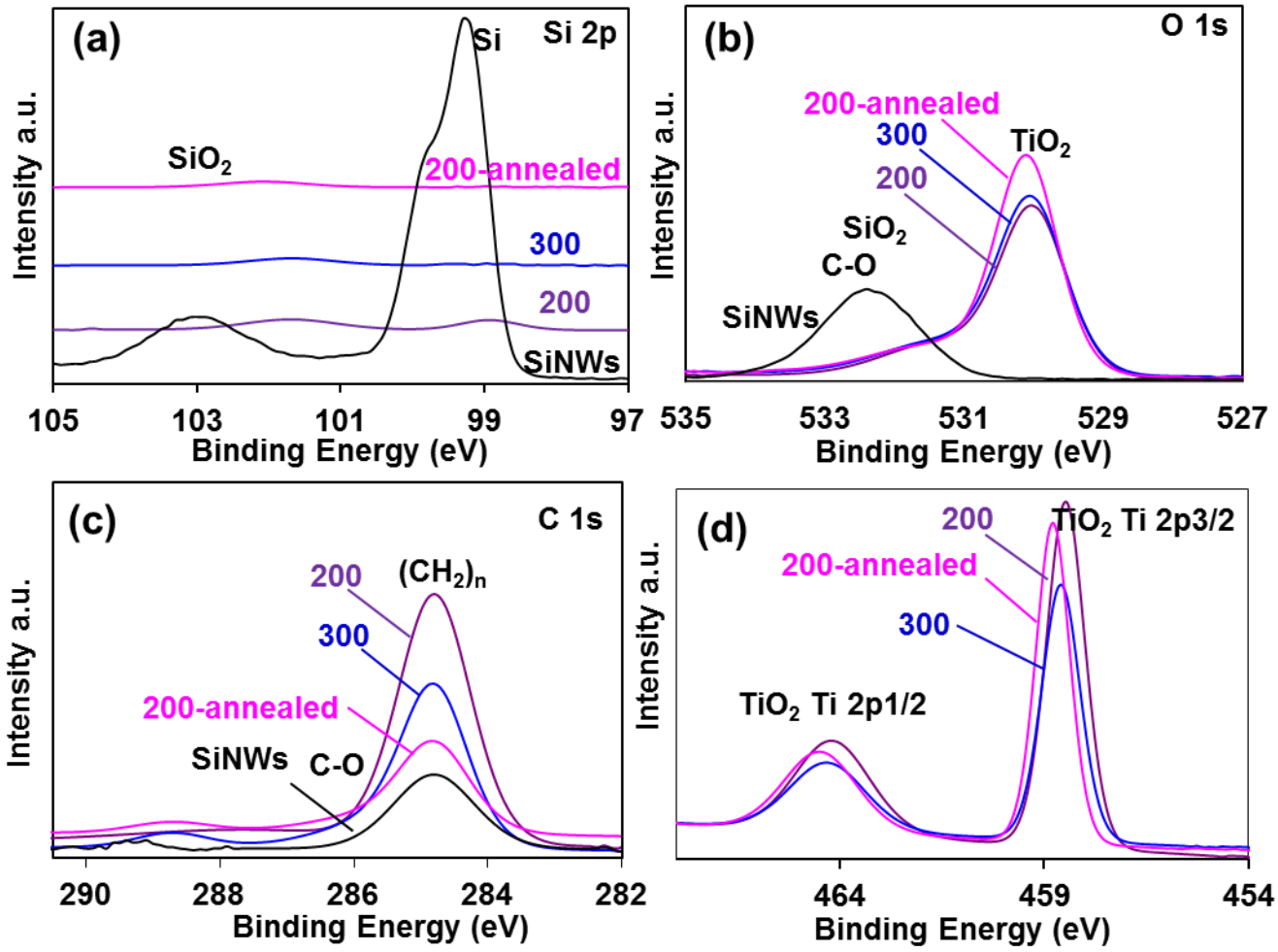

Figure S4: C1s, Si1s, O1s and Ti 2p XPS spectra of as-synthesized SiNWs, (10)TiO_2/SiNWs at ALD deposition temperatures of 200 and 300 °C and after annealing.

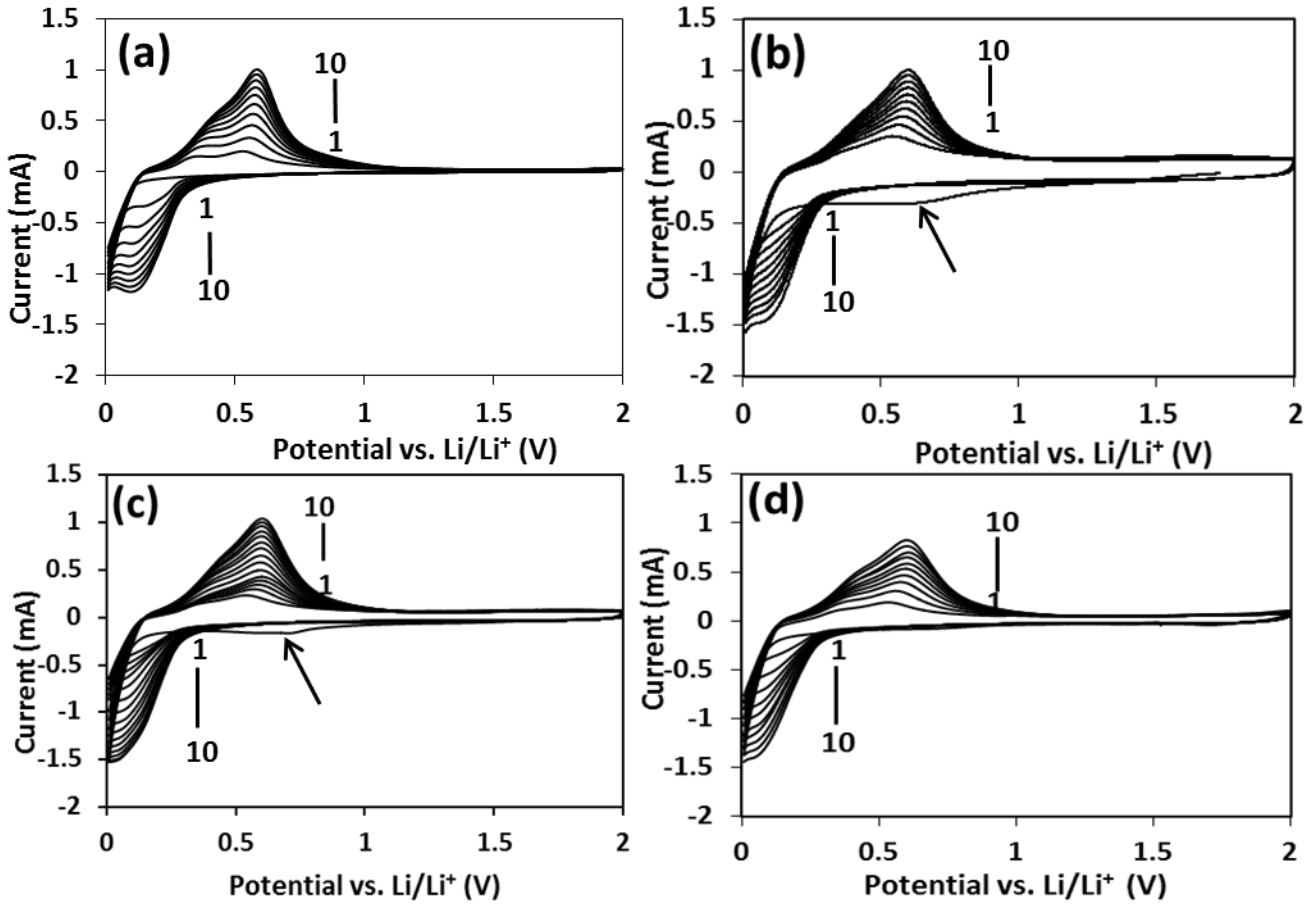

Figure S5: CV curves of (a), bare SiNWs, (b) (10)TiO_2-200/SiNWs, (c) (10)TiO_2-300/SiNWs and (d) (10)TiO_2-200(A)/SiNWs between 0.01 and 2V at a scan rate of 1 mV/s.

Comparing the CV curves of bare SiNWs and TiO_2-coated composites it can be seen that TiO_2 coating increases the current densities close to 0V slightly, indicating improved kinetics. For (10)TiO_2-200/SiNWs and (10)TiO_2-300/SiNWs there is a large, broad feature, indicated by the arrows, that is only found in the first cycle. Especially for (10)TiO_2-200/SiNWs, the current does not go to zero at higher potentials the way it does for bare SiNWs. This indicates that the TiO_2 coatings remain electrochemically active over a wide potential range (see also Figure S6 and S11).

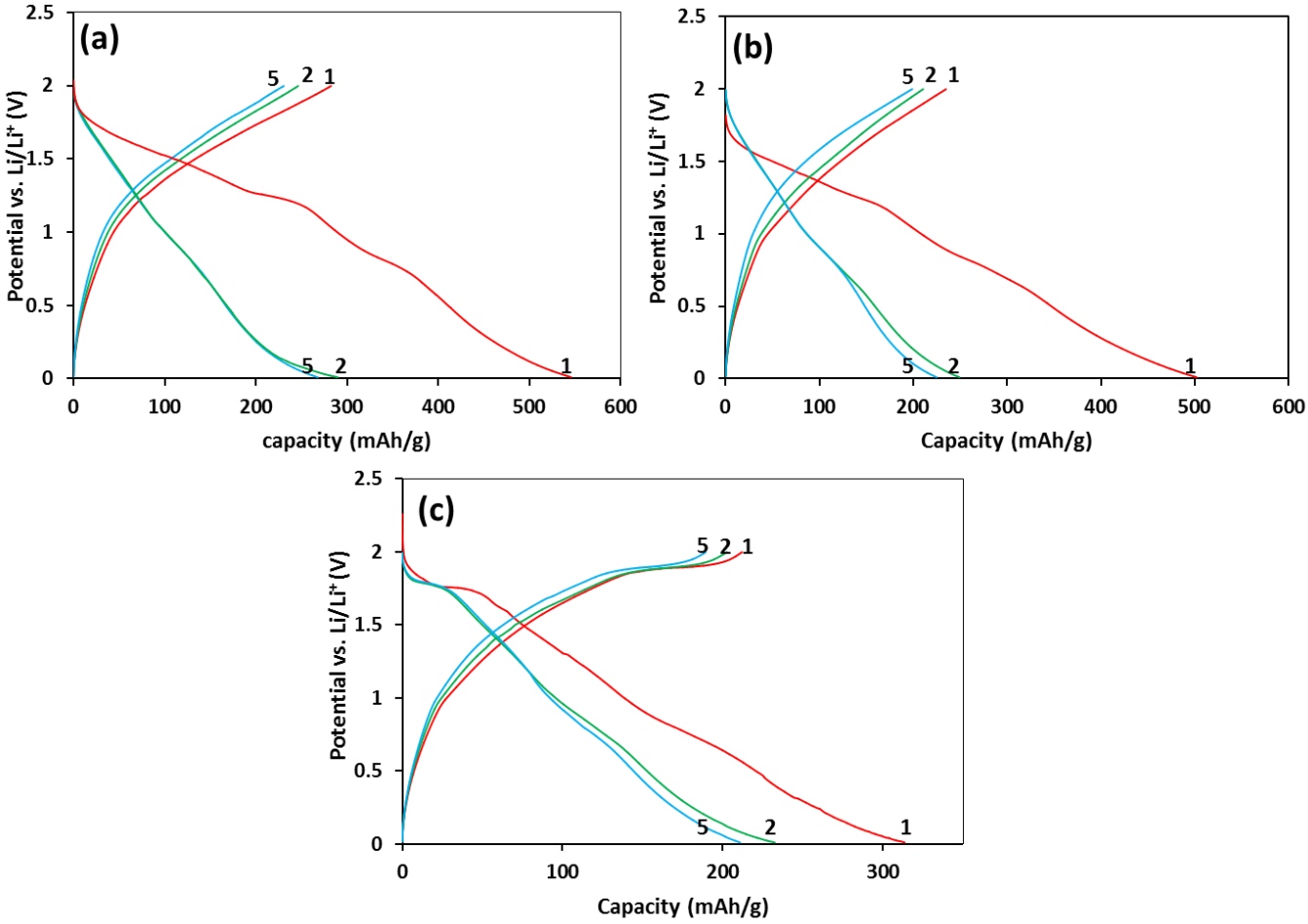

Figure S6: Galvanostatic discharge/charge curves of 10 nm TiO_2 at ALD deposition temperature of (a) 200 °C (b) 300 °C, (c) after annealing treatment at 600 °C for 1 hr at 0.1 C-rate.

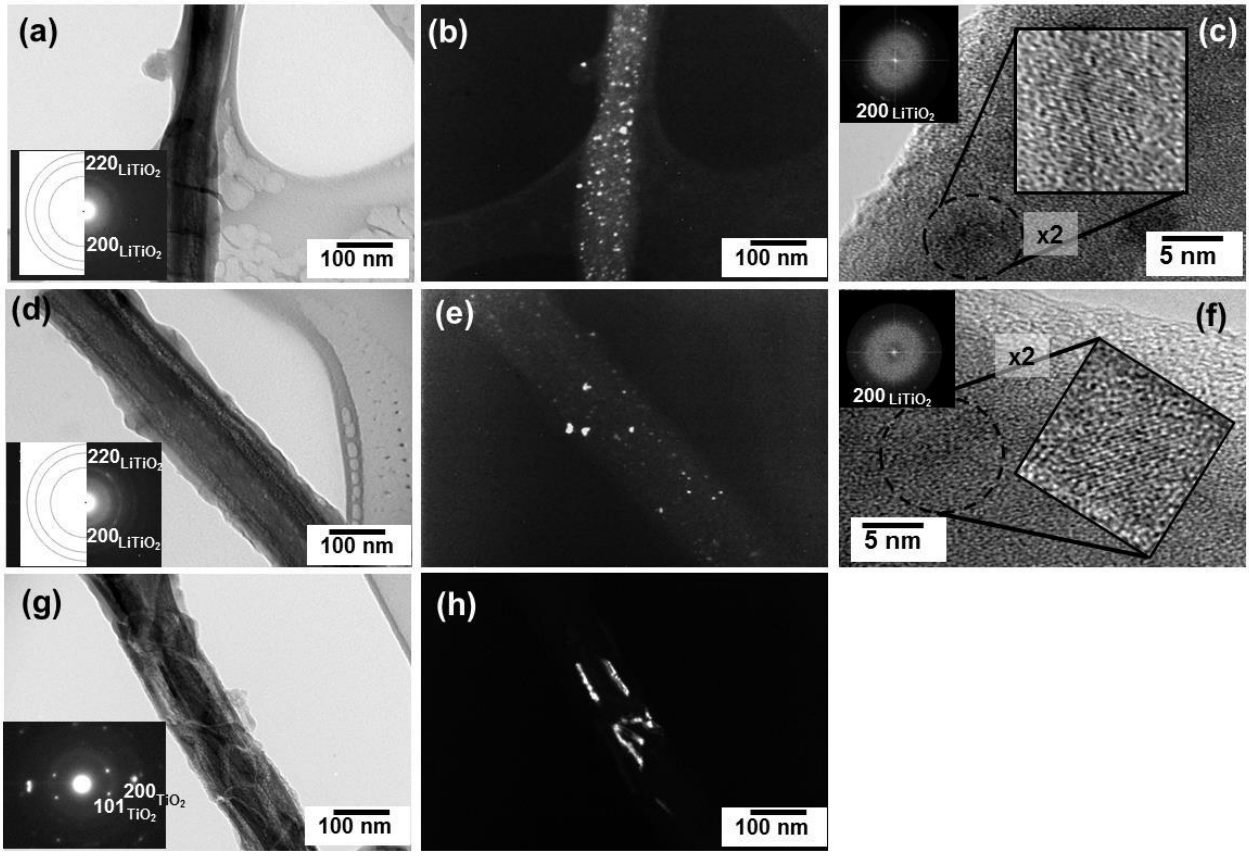

Figure S7. TEM micrographs of (a)-(c) (10)TiO_2-200/SiNWs, (c)-(f) (10)TiO_2-300/SiNWs, (g) and (h) (10)TiO_2-200(A)/SiNWs after 1 cycle (after delithiation to 2 V). (a), (d) and (g) bright field micrographs with corresponding selected area diffraction (SAD) insert. (b), (e) dark field micrographs using a portion of 200 $_{LiTiO2}$ ring pattern, highlighting coarser grain size of $LiTiO_2$ in (d). (f) dark field micrograph of the TiO_2 obtained using g=101$_{TiO2}$. HRTEM images of (c) (10)TiO_2-200/SiNWs, and (f) (10)TiO_2-300/SiNWs, highlighting partial crystallization of $LiTiO_2$ phase embedded in the amorphous region.

TEM micrographs of the three different coated composites after the first cycle are shown in Figure S7. The single-crystal diffraction pattern of Si is no longer found as nanowires become amorphous after 1 full lithiation/delithiation cycle[i]. The SAD pattern of TiO_2-200/SiNWs (Figure S7a) shows evidence of a cubic structure and the calculated d-spacings are 0.204, 0.146 nm, which correspond to cubic lithium titanate ($LiTiO_2$)[ii]. The HRTEM image in Figure S7c confirms the presence of crystalline $LiTiO_2$ phase embedded in the remaining amorphous phase. The lattice fringe spacing is 0.204 nm, corresponding to the (200) planes of cubic $LiTiO_2$. Also for (10)TiO_2-300/SiNWs, the $LiTiO_2$ phase is found with identical lattice spacings as for (10)TiO_2-200/SiNWs.

The dark-field images in Figure S7 (b) and (e), taken using a portion the 200 $LiTiO_2$ diffraction ring, show a larger grain size of the $LiTiO_2$ phase for TiO_2-300/SiNWs, likely due to

the higher residual precursor content at 200°C. Higher deposition temperatures are also reported to lead to slightly more dense coatings, irrespective of precursor residues[iii], which may also contribute to the difference in $LiTiO_2$ grain size. The SAD pattern of TiO_2-200(A)/SiNWs only shows diffraction spots related to the anatase phase and no evidence for $LiTiO_2$ was found (Figure S7g). The dark field image in Figure S7h is taken from the g=101 anatase TiO_2.

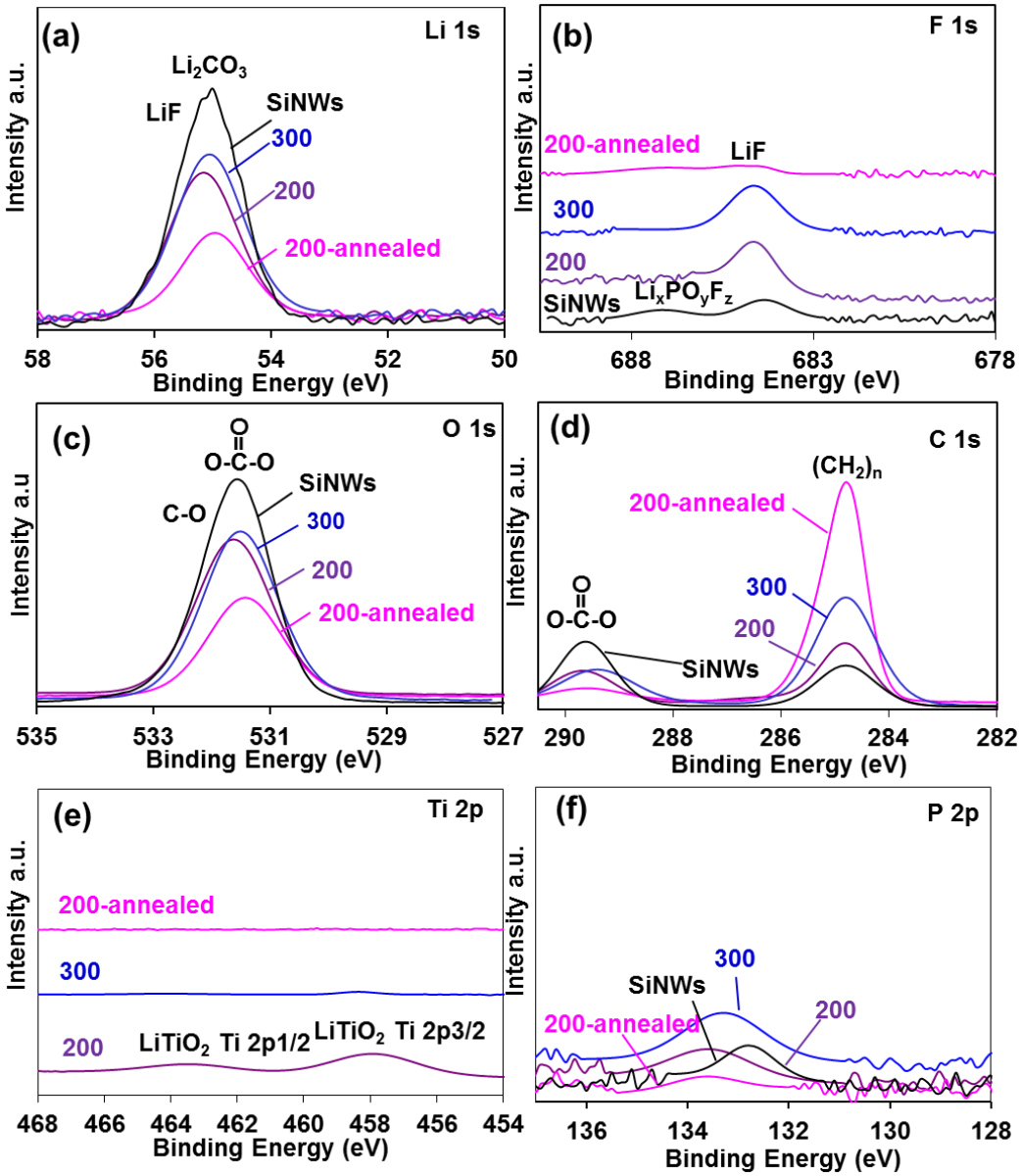

Figure S8. XPS spectra for bare SiNW electrode and electrodes coated with 10 nm TiO_2 after the first cycle.

The Li and C1s spectra in Figure S8 clearly show higher Li signal and higher amount of Li_2CO_3 for bare SiNWs compared to coated composites, despite the higher LiF content for the coated

materials, showing the passivating effect of the TiO_2. Table S1 show that the relative Li content decreases from 1 to 100 cycles for all electrodes except (10)TiO_2-200(A)/SiNWs, indicating that more Li_2CO_3 forms in the early stages of cycling and more single-electron reduction products such as Li alkylcarbonates and alkoxides form in later cycles.

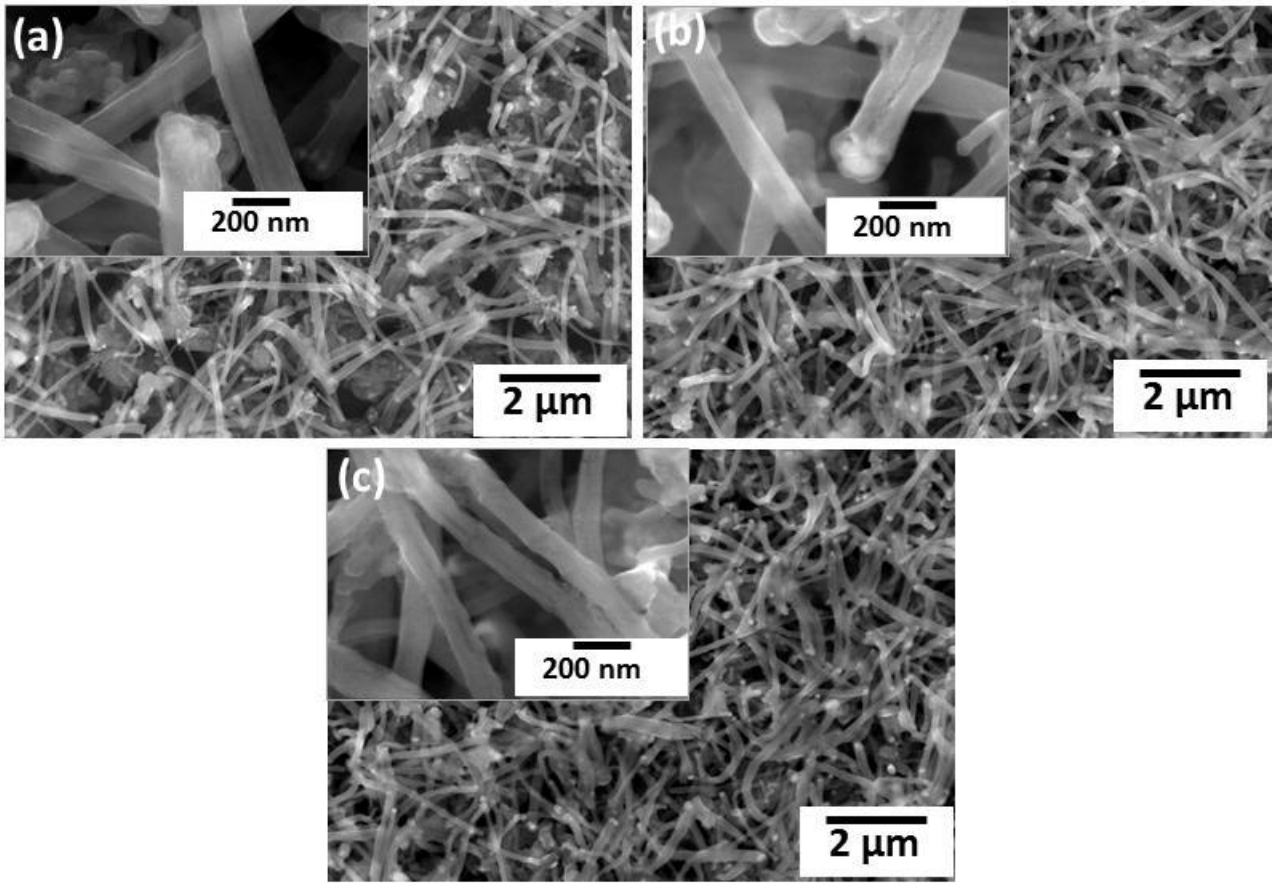

Figure S9: SEM images of (a) (10)TiO_2-200/SiNWs, (b) (10)TiO_2-300/SiNWs and (c) (10)TiO_2-200(A)/SiNWs after the first cycle at 0.1 C-rate.

SEM images of SiNWs coated with amorphous and crystalline TiO_2 show near-identical morphology after the first cycle (charge to 2 V). All electrodes have collected only a small amount of SEI. This agrees well with the small differences in first-cycle CE that were found (see Table 1) and the electrochemical measurements that indicated that most of the differences between the electrodes are due to differences in (ir)reversibility of the lithiation of the TiO_2 coating itself.

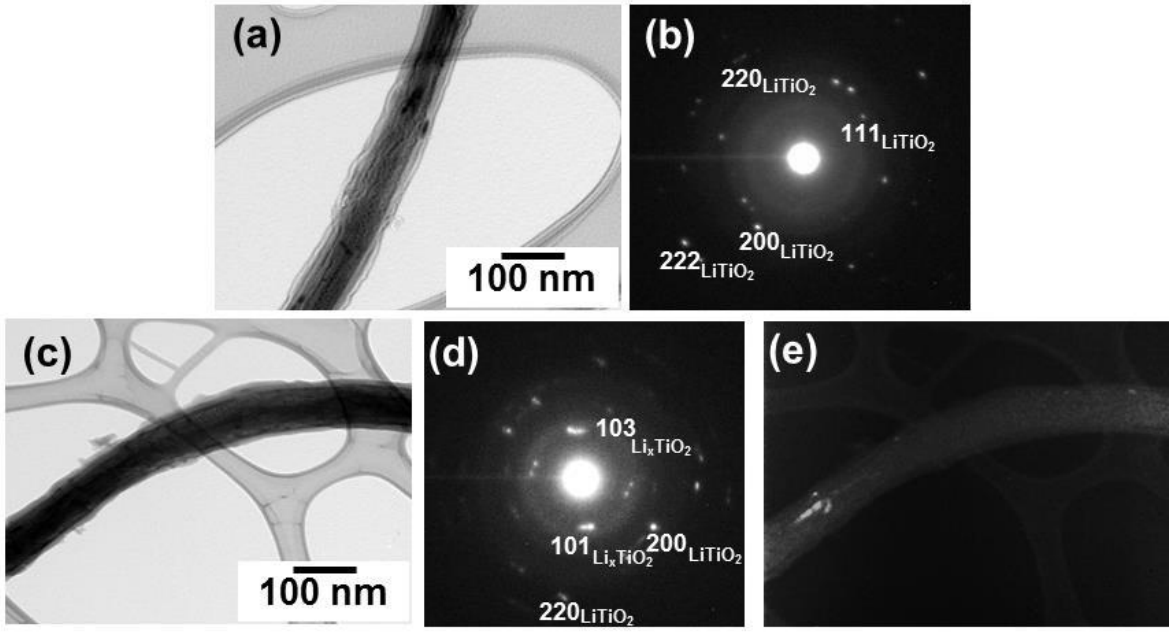

Figure S10. (a) bright-field image of (10)TiO_2-200/SiNWs after 1 cycle between 0.01 and 3V vs. Li/Li^+ (b) corresponding SAD pattern confirming the cubic structure. (c)-(e) TEM micrographs of TiO_2-200(A)/SiNWs after 35 cycles (after lithiation to 0.01 V). (c) Bright field micrograph, (d) corresponding indexed selected area diffraction (SAD) pattern, (c) dark field micrograph using $g=101_{LixTiO2}$, (e) dark field micrograph obtained using $g=200_{LiTiO2}$.

Even after delithiating up to +3V vs. Li/Li^+, cubic $LiTiO_2$ persists in (10)TiO_2-200/SiNWs. A small amount of $LiTiO_2$ is also formed in anatase TiO_2 as the dark-field micrograph of in Fig. S10e shows, but contrary to (10)TiO_2-200/SiNWs and (10)TiO_2-300/SiNWs, it does not persist in the delithiated state (see Figure S7).

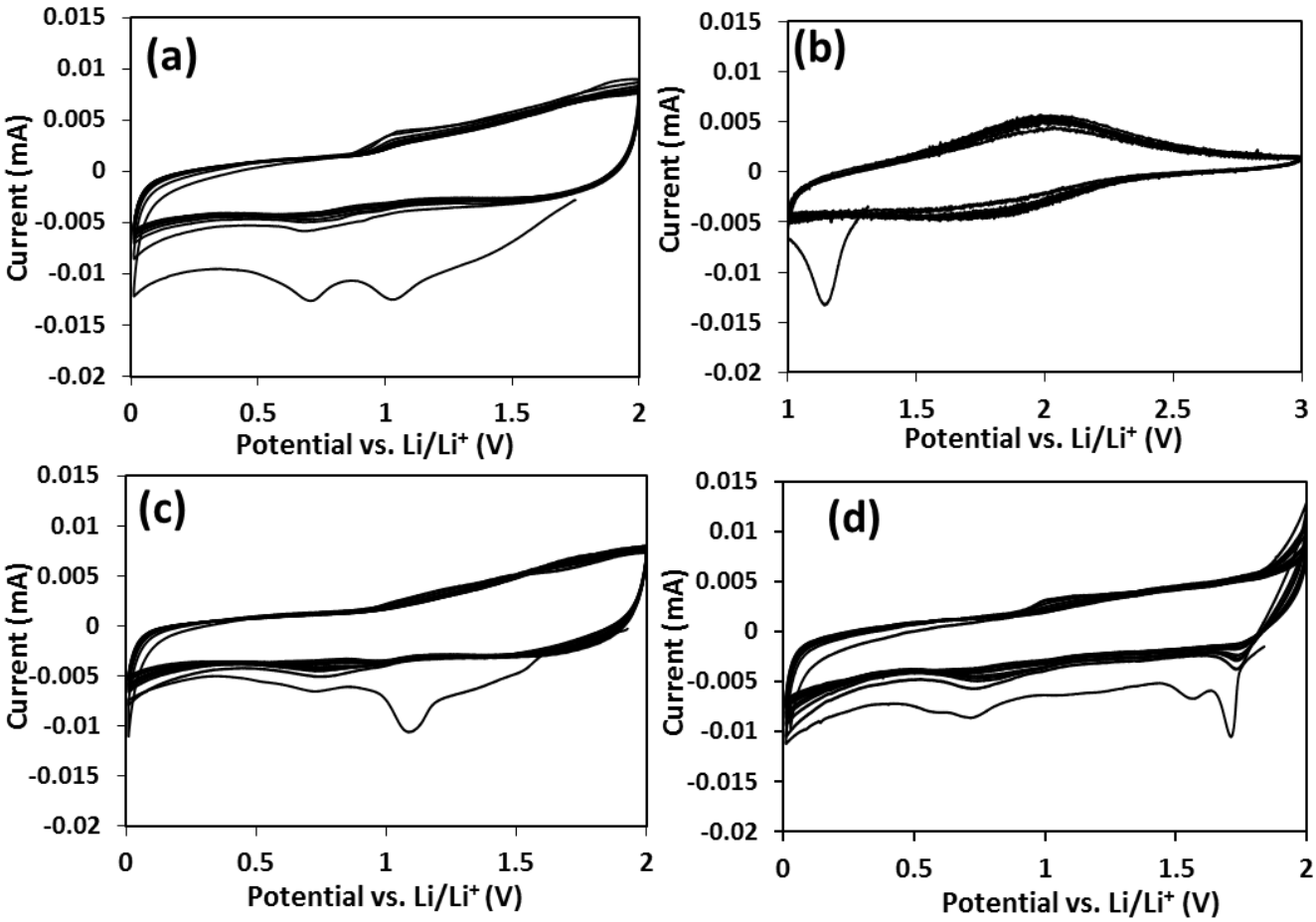

Figure S11: CV curves of planar TiO_2 films (a), deposited at 200°C between 0.01 and 2V and (b) between 1 and 3 V vs. Li/Li^+, (c) deposited at 300°C and (d) annealed at 600°C between 0.01 and 2V at a scan rate of 0.2 mV/s.

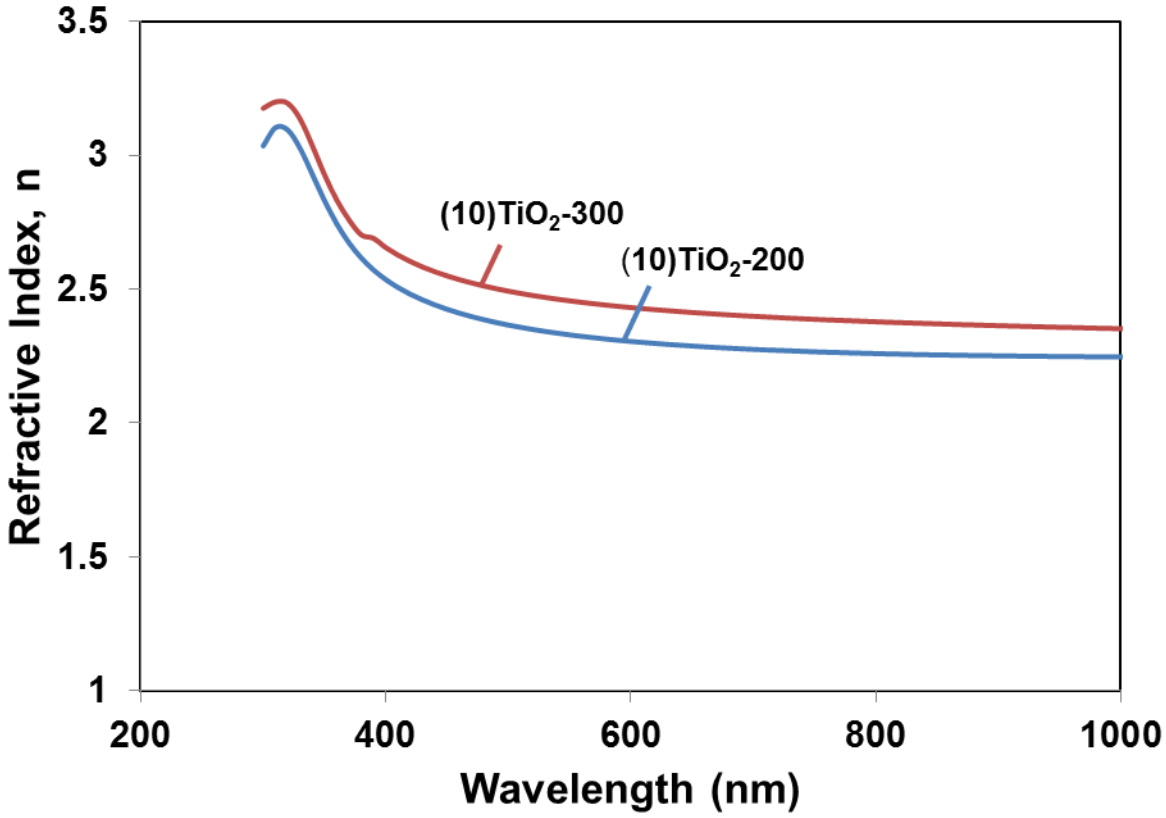

Figure S12: Refractive index as a function of wavelength for 10 nm planar TiO_2 films on Si deposited at 200 and 300°C

Figure S12 shows the refractive index measured as a function of wavelength for planar 10 nm TiO_2 deposited with ALD at 200 and 300°C. The higher refractive index for the film deposited at 300°C is closer to the bulk value for anatase, indicating slightly higher density for this film compared to the one deposited at 200°C.

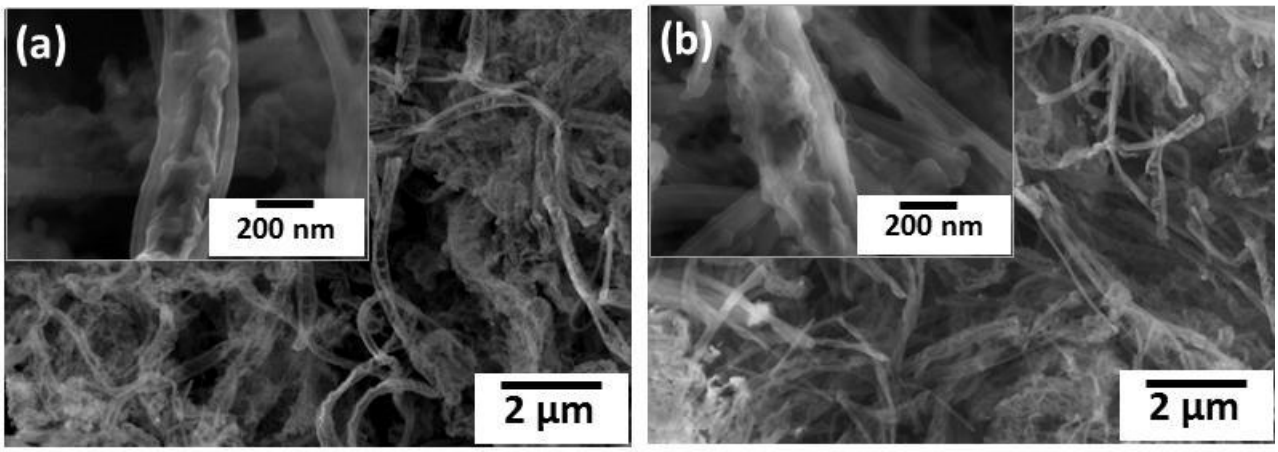

Figure S13: SEM images of (a) (5)TiO_2-200/SiNWs, (b) (15)TiO_2-200/SiNWs at 0.1 C-rate after 100 cycles

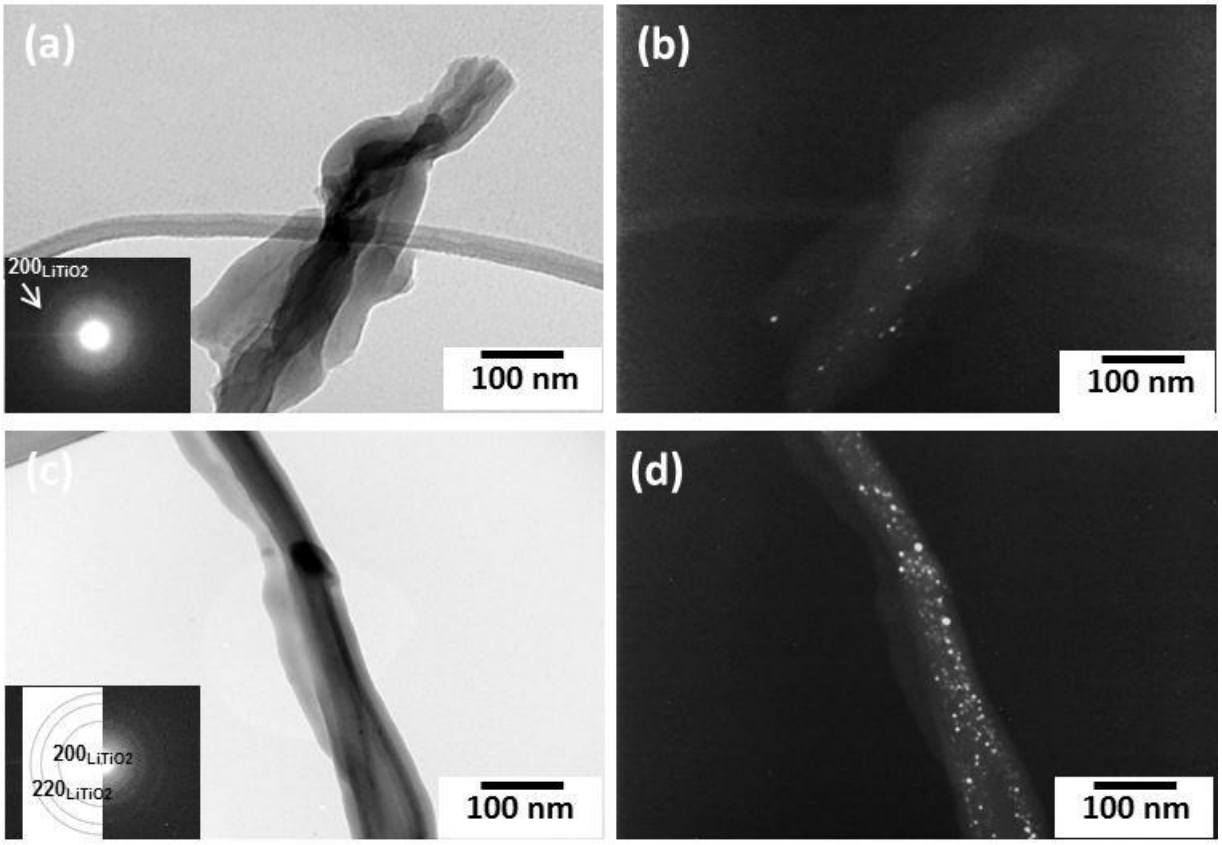

Figure S14: TEM micrographs of (a) and (b) (5)TiO_2-200/SiNWs, (c) and (d) (15)TiO_2-200/SiNWs after 100 cycles. (a) and (c) are bright field micrographs with corresponding SAD insert. (b), and (d) dark field micrographs obtained using a portion of the 200_{LiTiO2} ring pattern.

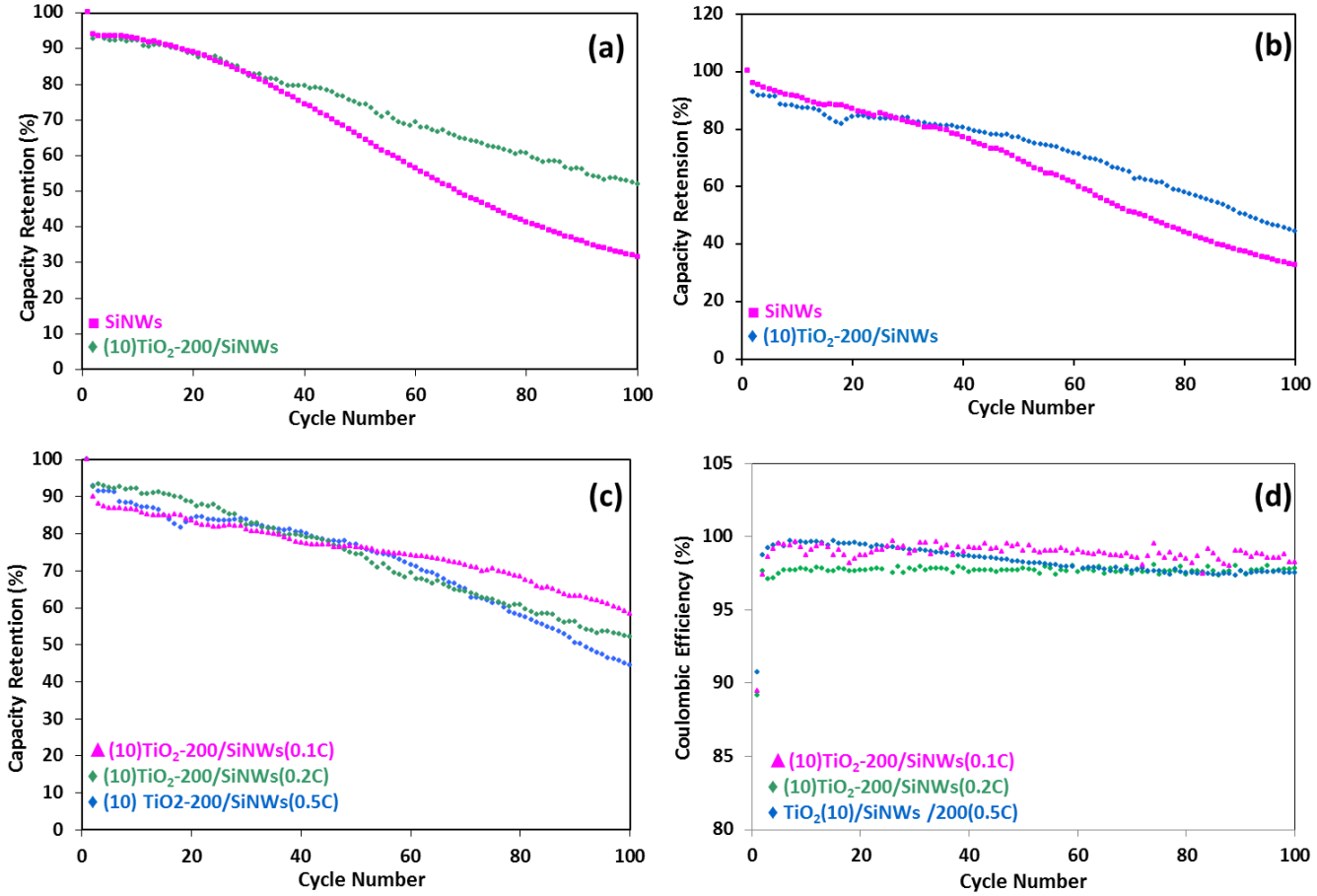

Figure S15: Capacity retention vs. cycle number for bare and (10)TiO_2-200/SiNWs nanocomposite at (a) 0.2 C-rate, (b) 0.5 C-rate, (c) Comparison of the % capacity retention of (10)TiO_2-200/SiNWs nanocomposite at different C-rates, and (d) comparison of the corresponding coulombic efficiency at different C-rates.

When cycling at higher rates, the capacity retention is worse than at 0.1 C, but still consistently better than for bare SiNWs. Combined with the SEM images in Figure S16, these results indicate that the coatings are more vulnerable to fracture and delamination at higher rates.

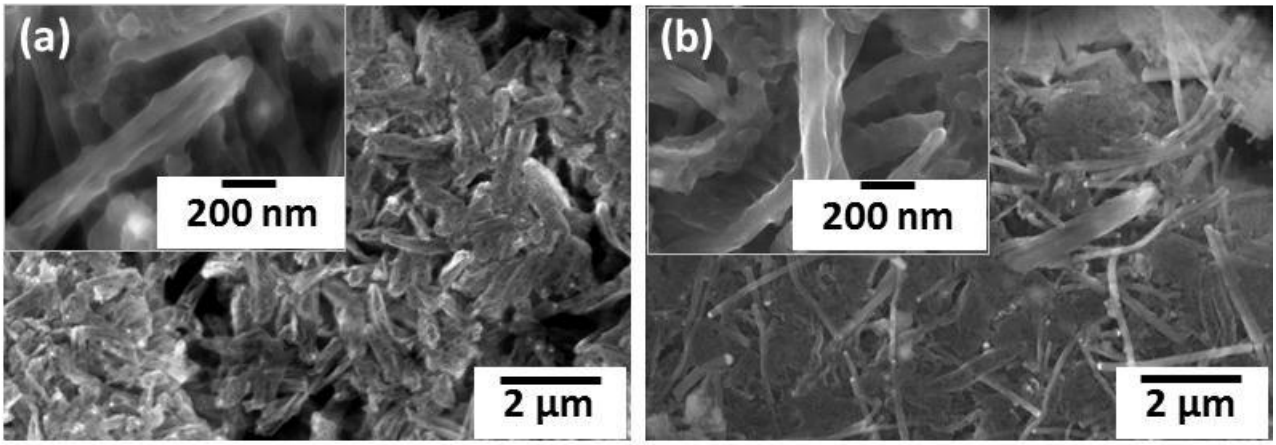

Figure S16: SEM images of (10)TiO_2-200/SiNWs at (a) 0.2 C-rate, (b) 0.5 C-rate after 100 cycles.

At higher rates, the nanowires show much higher degree of agglomeration and SEI formation, consistent with the lower CE and cycling stability in Figure S15.

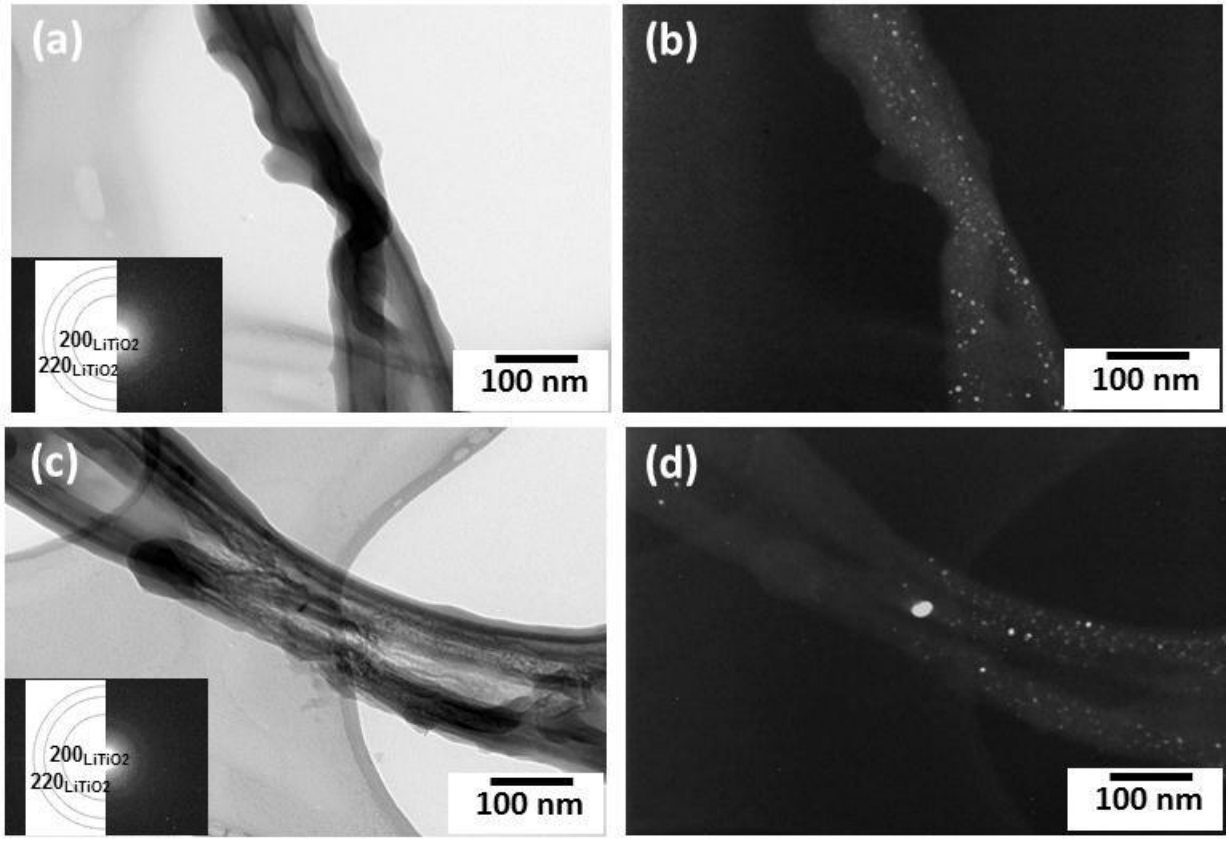

Figure S17: TEM micrographs of (10)TiO_2-200/SiNWs at (a) and (b) 0.2 C-rate, (c) and (d) 0.5 C-rate after 100 cycles. (a), and (c) bright field micrographs with corresponding SAD pattern insert. (b), and (d) dark field micrographs obtained using a portion of 200_{LiTiO2} ring pattern.

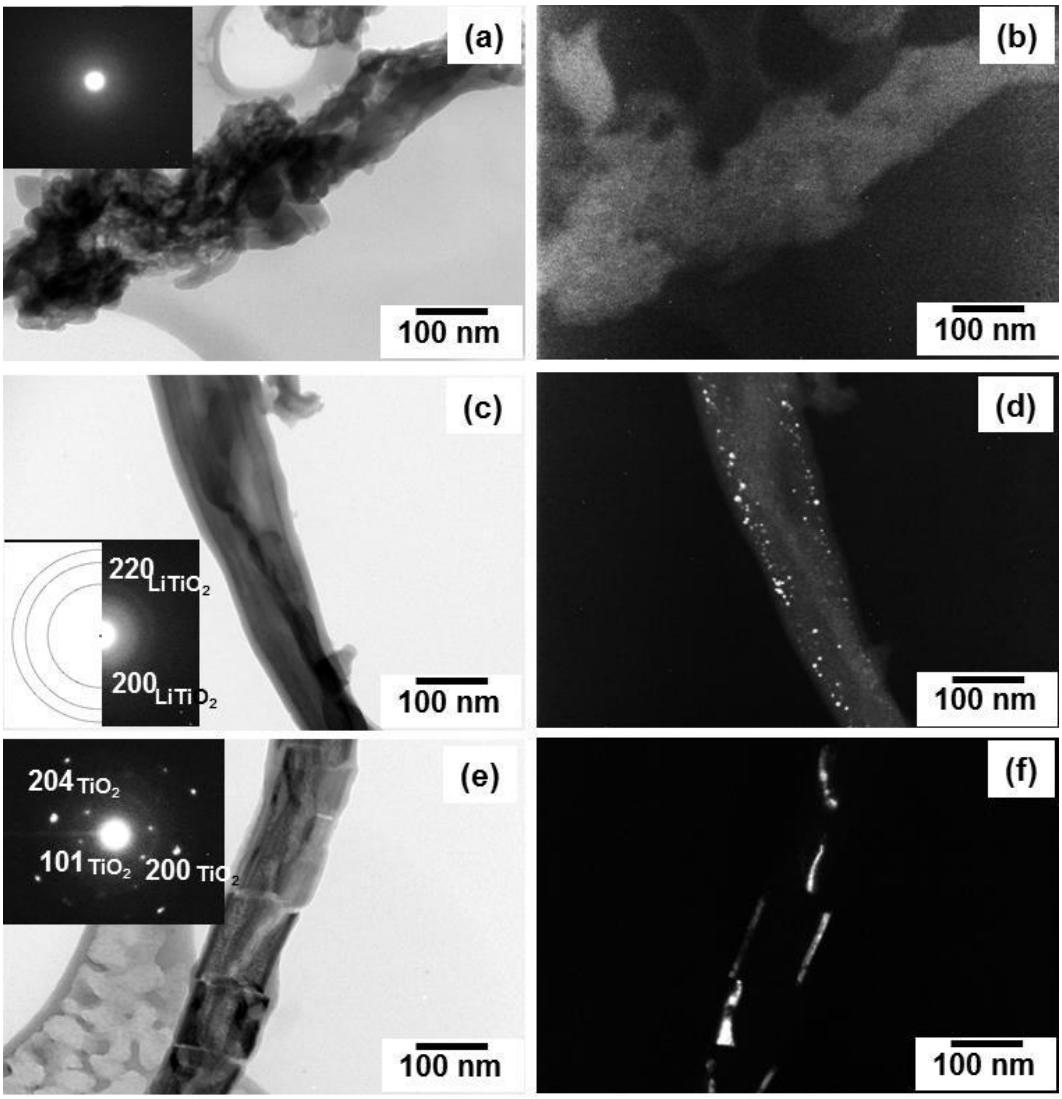

Figure S18 (a) TEM micrographs of (a) and (b) bare SiNWs, (c) and (d) (10)TiO_2-200/SiNWs and (e) and (f) (10)TiO_2-200(A)/SiNWs after 100 cycles at different rates according to Figure 3d (after delithiation to 2 V). (a), (c) and (e) bright field micrographs with corresponding SAD insert. (b), dark field micrograph using a portion of diffuse ring, (d) dark field micrographs using a portion of 200_{LiTiO2} ring pattern, and (f) dark field micrographs using g=101_{TiO2}.

As expected, bare nanowires have been completely disintegrated and the original shape of the nanowires has not been preserved. The coating with two-phase nanostructure consisting of $LiTiO_2$ and amorphous TiO_2, which has formed from the primary amorphous TiO_2 after the first cycle, is still intact, whereas, the anatase TiO_2 shell with large grains has been broken into several fragments.

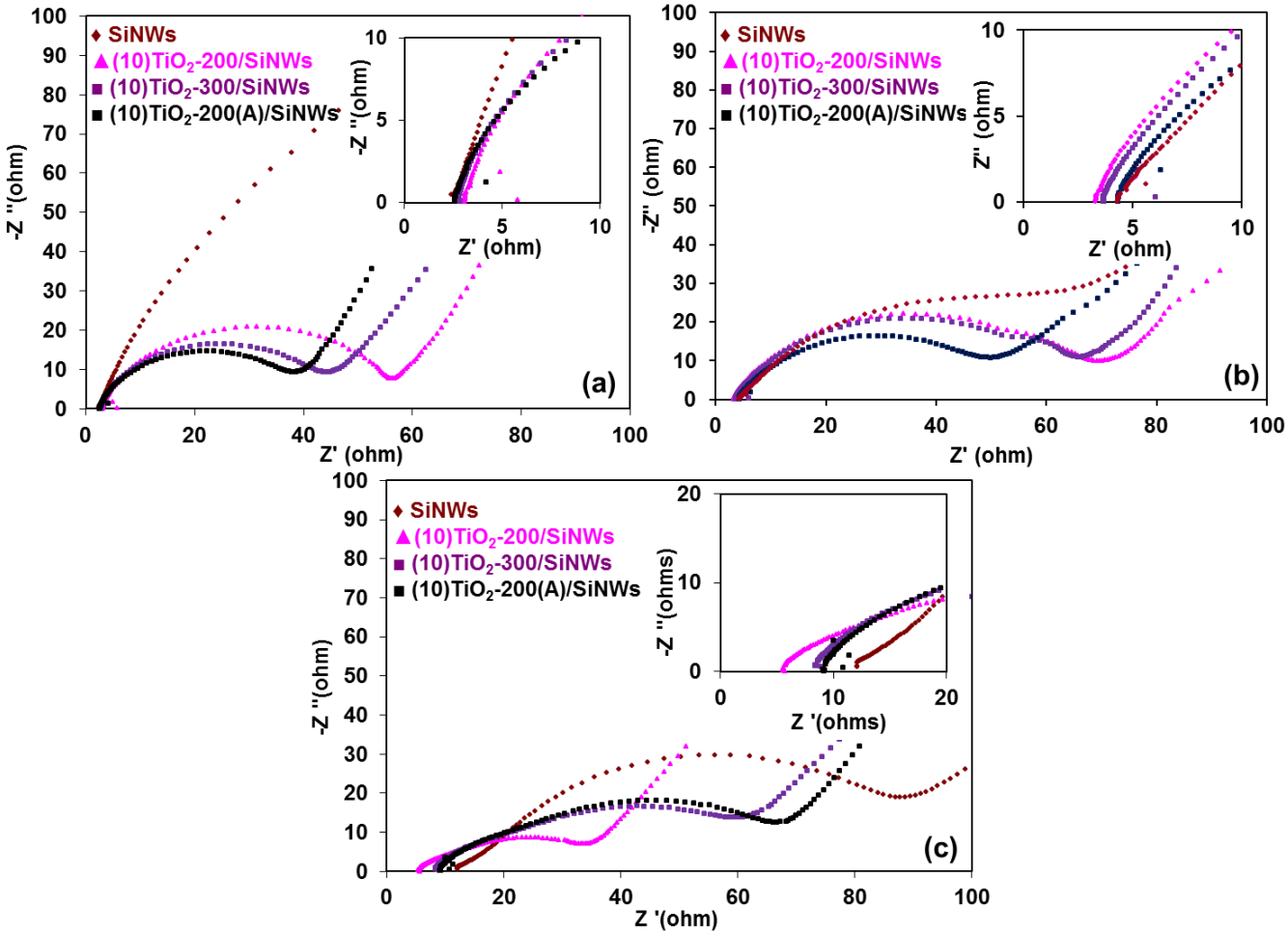

Figure S19: Impedance spectra of SiNWs and TiO_2/SiNWs nanocomposites (a) as-synthesized, (b) after 1st cycle, and (c) after 100 cycles after delithiation

From the impedance spectra, a number of differences between the composites are obvious. Native oxide on bare SiNWs causes the charge transfer resistance to be very high (a). The TiO_2 coatings have much lower reaction resistance possibly related to its lower bandgap (3.5 eV vs. 9 eV for SiO_2) and a difference in activation energy between an intercalation (TiO_2) and a conversion (SiO_2) reaction. All spectra are shifted along the real axis by ~3 Ohm. This is the sum of the resistances of the electrical connections in the experimental setup. The conductive pathways from the substrate to the nanowire surfaces and ionic diffusion through the electrolyte also add to this resistance. After 100 cycles, all the spectra show a larger shift along the real axis compared to the as-synthesized state, due to SEI formation on the working (i.e. SiNW) electrode. The spectrum for bare SiNWs is shifted by a considerably larger amount than that of (10)TiO_2-200/SiNWs reflecting differences in the amount of SEI build-up.

[i] Memarzadeh, E. L.; Kalisvaart,W. P.; Kohandehghan, A.; Zahiri,B.; Holt, C. M. B.; Mitlin, D. *J. Mater. Chem*., **2012**, *22*, 6655-6668

[ii] Wang, D.; Choi, D.; Yang, Z.; Viswanathan, V. V.; Nie, Z.; Wang, C.; Song, Y.; Zhang, J. G.; Liu, J. *Chem. Mater*. **2008**, *20*, 3435–3442.

[iii] Huang, Y.; Pandraud, G.; Sarro, P. M. *J. Vac. Sci. Technol. A*, **2013**, *31*, 01A148